The Astrophysical Journal Supplement Series, 254:28 (14pp), 2021 June https://doi.org/10.3847/1538-4365/abef65

The GBT Diffuse Ionized Gas Survey (GDIGS): Survey Overview and First Data Release

L. D. Anderson[1,2,3], Matteo Luisi[1,3], Bin Liu[1,4,5], Trey V. Wenger[6], Dana. S. Balser[7], T. M. Bania[8], L. M. Haffner[9], Dylan J. Linville[1,3], and J. L. Mascoop[1,3]
[1] Department of Physics and Astronomy, West Virginia University, Morgantown, WV 26506, USA; loren.anderson@mail.wvu.edu
[2] Green Bank Observatory, P.O. Box 2, Green Bank, WV 24944, USA
[3] Center for Gravitational Waves and Cosmology, West Virginia University, Chestnut Ridge Research Building, Morgantown, WV 26505, USA
[4] National Astronomical Observatories, Chinese Academy of Sciences, Beijing 100012, People's Republic of China
[5] CAS Key Laboratory of FAST, NAOC, Chinese Academy of Sciences, People's Republic of China
[6] Dominion Radio Astrophysical Observatory, Herzberg Astronomy and Astrophysics Research Centre, National Research Council, P.O. Box 248, Penticton, BC V2A 6J9, Canada
[7] National Radio Astronomy Observatory, 520 Edgemont Road, Charlottesville, VA 22903, USA
[8] Institute for Astrophysical Research, Astronomy Department, Boston University, 725 Commonwealth Avenue, Boston, MA 02215, USA
[9] Department of Physical Sciences, Embry-Riddle Aeronautical University, Daytona Beach, FL 32114, USA
Received 2021 January 22; revised 2021 March 12; accepted 2021 March 15; published 2021 May 24

Abstract

The Green Bank Telescope (GBT) Diffuse Ionized Gas Survey (GDIGS) traces ionized gas in the Galactic midplane by measuring 4–8 GHz radio recombination line (RRL) emission. The nominal survey zone is $32\overset{\circ}{.}3 > \ell > -5^{\circ}$, $|b| < 0\overset{\circ}{.}5$, but coverage extends above and below the plane in select fields and additionally includes the areas around W47 ($\ell \simeq 37\overset{\circ}{.}5$) and W49 ($\ell \simeq 43^{\circ}$). GDIGS simultaneously observes 22 Hnα (15 usable), 25 Hnβ (18 usable), and 8 Hnγ RRLs (all usable), as well as multiple molecular line transitions (including those of $H_2^{13}CO$, H_2CO, and CH_3OH). Here, we describe the GDIGS survey parameters and characterize the RRL data, focusing primarily on the Hnα data. We produce sensitive data cubes by averaging the usable RRLs, after first smoothing to a common spectral resolution of 0.5 km s^{-1} and a spatial resolution of $2\overset{\prime}{.}65$ for Hnα, $2\overset{\prime}{.}62$ for Hnβ, and $2\overset{\prime}{.}09$ for Hnγ. The average spectral noise per spaxel in the Hnα data cubes is $\sim$10 mK ($\sim$5 mJy beam^{-1}). This sensitivity allows GDIGS to detect RRLs from plasma throughout the inner Galaxy. The GDIGS Hnα data are sensitive to emission measures EM $\gtrsim$ 1100 cm^{-6} pc, which corresponds to a mean electron density $\langle n_e \rangle \gtrsim 30$ cm^{-3} for a 1 pc path length or $\langle n_e \rangle \gtrsim 1$ cm^{-3} for a 1 kpc path length.

Unified Astronomy Thesaurus concepts: Warm ionized medium (1788); Interstellar plasma (851); H II regions (694); Interstellar line emission (844)

1. Introduction

The myriad Galactic plane surveys undertaken over the last decades have given us a clear view of nearly all the components of the Milky Way disk. These surveys cover the visible through radio regimes, tracing stars (2MASS, UKIDSS), warm dust (MSX, Spitzer GLIMPSE and MIPSGAL), cold dust (Herschel Hi-Gal, AKARI, ATLASGAL, BGPS), compact ionized gas (SUMSS, MAGPIS, CORNISH), H I (IGPS), and molecular gas (e.g., GRS, HOPS, SPLASH). The major omission, however, is data that are sensitive to 10^4 K "diffuse ionized gas" (DIG) in the Galactic plane. The DIG, sometimes called the "warm ionized medium" or "WIM" is a low-density plasma whose existence was first proposed by Hoyle & Ellis (1963). It is a major component of the interstellar medium (ISM), making up $\sim$20% of the total Milky Way gas mass and $\gtrsim$90% of its ionized gas mass (Reynolds 1991) and providing a major source of pressure at the midplane (Boulares & Cox 1990). Although we have known about the DIG for over half a century and it is a major component of the ISM, there remain major unanswered questions regarding its origin, distribution, and characteristics. We cannot therefore fully trace the recycling of material that takes place in the ISM, nor can we develop a complete picture of how star formation impacts the ISM of our Galaxy.

The DIG exists in a variety of environments and hence has a range of densities. In the immediate vicinity of a H II region, but outside its photodissociation region (PDR), there often exists an ionized gas "halo" (Anantharamaiah 1985, 1986). These halos may be due to photons leaking through the H II region PDRs, as has been shown for the H II regions RCW 120 (Anderson et al. 2015a) and NGC 7538 (Luisi et al. 2016). Pellegrini et al. (2020) modeled the emission from H II regions in a Milky Way–like galaxy and found that their halos were bright due to leakage. There also is widespread lower density ionized gas in the Milky Way disk that cannot definitively be associated with any individual H II region (e.g., Geyer & Walker 2018). Here, we refer to all diffuse ionized gas outside of H II regions as the "DIG."

Extragalactic studies of the DIG have benefited from recent hardware advances that allow for two-dimensional mapping using integral field units such as SAURON (Bacon et al. 2001), SparsePak (Bershady et al. 2005), PMAS (Roth et al. 2005), VIRUS-P (Hill et al. 2008), MUSE (Bacon et al. 2010), and MaNGA (Bundy et al. 2015). These instruments can map the emission from galaxies quickly and determine their ionized gas properties. The forthcoming Local Volume Mapper (Kollmeier et al. 2017) of the Sloan Digital Sky Survey (SDSS; Gunn et al. 2006) will allow for $\sim 2 \times 10^7$ simultaneous spectra to be taken, allowing plasma diagnostics over a range of physical scales.

Most studies of the Milky Way DIG have been conducted by observing Hα emission. Although Hα is very bright compared to other ionized gas tracers, it suffers from extinction. This drastically limits the distance to which the DIG in the inner Galaxy can be studied. The all-sky Hα WHAM survey (Reynolds et al. 1998; Haffner et al. 2003) gives us a clear

view of the global properties of diffuse ionized gas. Due to extinction and its relatively coarse resolution of ∼1°, however, WHAM data cannot be used for detailed studies of the inner Galaxy midplane where significant diffuse ionized gas resides.

The Milky Way DIG can also be studied using far-infrared (FIR) fine-structure lines. Unlike Hα, such lines do not suffer from extinction. To date, however, such studies have been limited to select sight lines or coarse maps, often at poor spectral resolution. For example, the only large-scale map extant is that of the [N II] 122 and 205 μm lines, mapped by the FIRAS instrument on the Cosmic Background Explorer (COBE) at 7° angular resolution and ∼700 km s^{-1} spectral resolution (Wright et al. 1991). Because the ionization potential of nitrogen is greater than that of hydrogen, the distribution of ionized nitrogen should be similar to that of ionized hydrogen; the lines of nitrogen are therefore the most useful FIR DIG tracers. Goldsmith et al. (2015) used Herschel observations of the 122 and 205 μm [N II] fine-structure lines along ∼150 lines of sight in the plane. They found electron densities $n_e \simeq$ 10–50 cm^{-3} and coined the phase for this plasma the "dense warm ionized gas," D-WIM. Pineda et al. (2019) extended this work to the analysis of 11 lines of sight in the plane and found electron densities $n_e \simeq$ 10–200 cm^{-3}. The electron densities derived in these studies are higher than those of extraplanar DIG (which has $n_e \simeq 0.1$ cm^{-3}; Haffner et al. 2009) and lower than those of most H II regions (e.g., the Orion nebula has $n_e \simeq 10^{2.3}$–$10^{4.5}$ cm^{-3}; Lockman & Brown 1975).

Observations of radio recombination lines (RRLs) give us an opportunity to investigate the Galactic midplane DIG distribution throughout the Galactic disk at high spatial and spectral resolution. RRLs are produced from recombining ions and electrons and are the higher quantum number corollaries to Hα emission. We therefore expect RRL emission from H II regions surrounding OB stars and from diffuse ionized gas. There are, however, few large-scale RRL surveys. Past RRL observations of the Galactic DIG (e.g., Roshi & Anantharamaiah 2000, 2001; Baddi 2012) found prevalent emission, but are inappropriate for detailed studies of the DIG due to poor angular resolution. The beam-sampled RRL survey SIGGMA has a sensitivity of ∼ 1 mJy beam^{-1} at 5 km s^{-1} spectral resolution and ∼3.′4 spatial resolution (Liu et al. 2013, 2019). SIGGMA is sensitive to discrete sources but due to the observing strategy has decreased sensitivity to extended emission over ∼1° in extent. In the only other large-scale RRL survey extant, Alves et al. (2015) report 6.4 mJy beam^{-1} sensitivity at 20 km s^{-1} spectral resolution. Both of these comparison surveys are near 1.4 GHz.

In previous RRL observations by our group, we serendipitously discovered prevalent, diffuse ionized gas in the Milky Way. We created the H II Region Discovery Survey (HRDS; Bania et al. 2010), an RRL survey of discrete H II regions throughout the Galactic disk. To date, we have discovered ∼1400 nebulae, approximately doubling the previously known sample in the Galaxy. Nearly 30% of all observed positions, however, have two or more distinct RRL velocities. We showed using subsequent observations that one of these components was from the DIG and the other was from the compact H II regions that we targeted (Anderson et al. 2015b). The multiple-velocity H II regions are rare at $\ell > 32°$, implying less diffuse ionized gas there. Our observations showed that diffuse ionized gas in the Galactic plane is easily detected by the Green Bank Telescope (GBT). With its 100 m diameter and unblocked aperture, the GBT has extraordinary surface brightness sensitivity, making it the ideal instrument for further studies of the DIG.

Table 1
GDIGS RRL Survey Parameters

Observing Parameters	
Observing dates	2016 July–December
Nominal coverage area	$32.^\circ3 > \ell > -5°$, $\lvert b\rvert < 0.^\circ5$
Usable frequencies	4.7–7.3 GHz
Mean Hnα frequency	5.7578 GHz
Hnα spatial resolution	2.′65
Integration time per Hnα beam	45 s
Mean Hnβ frequency	5.7959 GHz
Hnβ spatial resolution	2.′62
Integration time per Hnβ beam	44 s
Mean Hnγ frequency	6.4528 GHz
Hnγ spatial resolution	2.′09
Integration time per Hnγ beam	28 s
Data Products	
LSR velocity range	−300 to +300 km s^{-1}
Pixel size	30″
Channel spacing	0.5 km s^{-1}
Median spectral Hnα rms noise	10.3 mK
Median spectral Hnβ rms noise	10.8 mK
Median spectral Hnγ rms noise	21.3 mK

Here, we report on a new fully sampled survey of RRL emission, the GBT Diffuse Ionized Gas Survey (GDIGS). The first GDIGS data on the giant H II region W43 were published by Luisi et al. (2020). The same observing mode was used to study the ionized gas of S235 by Anderson et al. (2019). This paper describes the data acquisition and reduction methodology and characterizes the GDIGS RRL data.

2. GDIGS Data Acquisition and Processing

GDIGS is optimized to provide sensitive RRL data of the DIG, at good spatial resolution. We use the GBT C band receiver, which operates from 4 to 8 GHz, in total-power mode. The C band receiver can tune to the largest number of usable RRLs of any GBT receiver, at spatial resolutions of ∼2′. The GDIGS coverage area includes the bulk of the midplane DIG emission observable by the GBT. We characterize the GDIGS RRL survey parameters in Table 1, which summarizes much of the discussion below.

The GDIGS data are taken in intensity units of antenna temperature (T_A, in kelvin). At C band, atmospheric effects are negligible, and therefore, no correction for atmospheric opacity is required. The unblocked aperture of the GBT provides a "clean" beam with rear spillover, ohmic loss, and blockage efficiencies near unity; therefore, the measured antenna temperature is roughly the same as the atmosphere-corrected antenna temperature, or $T_A \simeq T_A^*$. For a point source, one can convert antenna temperature in Kelvin to flux density in Jansky using 2.0 K Jy^{-1} (Ghigo et al. 2001).[10] We can also convert the antenna temperature into the physical units of emission measure, EM $= \int n_e^2 dl$ (see Appendix A). Assuming an

[10] See also https://www.gb.nrao.edu/GBT/DA/gbtidl/gbtidl_calibration.pdf.

electron temperature of 8000 K, a line width $\Delta V = 25$ km s^{-1}, and the mean GDIGS Hnα frequency of 5.7578 GHz (see Equation (A7)):

$$\frac{\mathrm{EM}}{\mathrm{pc\ cm^{-6}}} = 176 \times 10^2 \frac{T_\mathrm{L}}{\mathrm{mK}}, \quad (1)$$

where T_L is the line intensity. Given the range of measured values for T_e and ΔV, we estimate that the relationship in Equation (1) has ∼100% uncertainty. In terms of the integrated intensity, using Equation (A8), the conversion for Hnα lines assuming an electron temperature of 8000 K is

$$\frac{\mathrm{EM}}{\mathrm{pc\ cm^{-6}}} = 6.39 \frac{W_\mathrm{RRL}}{\mathrm{mK\ km\ s^{-1}}}. \quad (2)$$

Based on the range of values for T_e in H II regions and the DIG, this expression has ∼50% uncertainties.

2.1. Observational Configuration

The Versatile GBT Astronomical Spectrometer (VEGAS) can simultaneously tune to 64 spectral windows at two orthogonal polarizations (*XX* and *YY*). Of these 64 tunings, we observe 22 Hnα lines from $n = 95$ to 117 (excluding H113α, which is compromised by the nearby H142β line). We observe 25 Hnβ lines from H120β to H146β (excluding H142β) and 8 Hnγ lines from H138γ to H147γ (excluding H142γ and H145γ). We also observe transitions of H_2CO, CH_2NH, HC_5N, CCS, C_3S, HC_9N_2, CH_3OH, HCN, $H_2^{13}CO$, and CH_3OH_3 (see Table 2 for transitions). The molecular line data will be discussed in subsequent publications. Each spectral window spans 23.4 MHz with a spectral resolution of 2.86 kHz. GDIGS also observes the total-power continuum intensity, which can be computed from the measured system temperatures. We are investigating whether the GDIGS continuum is a reliable data product.

In this observational configuration, the baseline stability is poor, and the system temperature is elevated below 4.7 GHz and above 7.3 GHz. This reduces the number of usable Hnα lines to 15 (H97α–H111α) and the number of usable Hnβ lines to 18 (H121β–H139β, excluding H137β, which is compromised by the 3(1, 2) → 3(1, 3) transition of CH_3OH_3). Over the range of usable transitions, the velocity resolution varies from 0.117 to 0.182 km s^{-1}, and the full velocity range per tuning varies from 961.6 to 1494 km s^{-1}.

We list the usable spectral lines in Table 2, which has columns of the line name, the transition, the line rest frequency, and the mean system temperature in the gridded maps (see Section 2.5). For all RRLs, in addition to the hydrogen lines, we also simultaneously observe in the same bandpasses the RRLs of helium and carbon, because they are shifted by ∼−120 and ∼−150 km s^{-1} from those of hydrogen, respectively. This configuration was first used by Anderson et al. (2018) and was also employed by Luisi et al. (2018, 2019).

2.2. Survey Strategy

GDIGS covers ∼49 deg^2, as shown in Figure 1. We describe the GDIGS data in this figure in later subsections. The nominal survey zone, spanning ∼37 deg^2, is $32.^\circ3 > \ell > -5^\circ$, $|b| < 0.^\circ5$. We also map 2 deg^2 in the area surrounding W47 ($38.^\circ0 > \ell > 37.^\circ0$, $1.^\circ5 > b > -0.^\circ5$) and 1 deg^2 in the area surrounding W49 ($43.^\circ5 > \ell > 42.^\circ5$, $|b| < 0.^\circ5$). Due to the extended emission in the Galactic center, we add ∼4 deg^2 of additional latitude coverage there. Finally, we provide a combined 5 deg^2 of additional latitude coverage within the

Table 2
Usable RRL and Molecular Line Transitions

Line	Transition	Frequency (GHz)	$\langle T_\mathrm{sys} \rangle$ (mK)
H97α	$n = 98 \rightarrow 97$	7.09541	43.8
H98α	$n = 99 \rightarrow 98$	6.88149	34.4
H99α	$n = 100 \rightarrow 99$	6.67607	30.7
H100α	$n = 101 \rightarrow 100$	6.47876	25.8
H101α	$n = 102 \rightarrow 101$	6.28914	25.5
H102α	$n = 103 \rightarrow 102$	6.10685	24.9
H103α	$n = 104 \rightarrow 103$	5.93154	24.5
H104α	$n = 105 \rightarrow 104$	5.76288	23.3
H105α	$n = 106 \rightarrow 105$	5.60055	23.3
H106α	$n = 107 \rightarrow 106$	5.44426	22.4
H107α	$n = 108 \rightarrow 107$	5.29373	24.8
H108α	$n = 109 \rightarrow 108$	5.14870	25.0
H109α	$n = 110 \rightarrow 109$	5.00892	24.3
H110α	$n = 111 \rightarrow 110$	4.87416	24.4
H111α	$n = 112 \rightarrow 111$	4.74418	24.9
H121β	$n = 123 \rightarrow 121$	7.24398	90.4
H122β	$n = 124 \rightarrow 122$	7.06882	60.5
H123β	$n = 125 \rightarrow 123$	6.89905	33.5
H124β	$n = 126 \rightarrow 124$	6.73479	32.6
H125β	$n = 127 \rightarrow 125$	6.57570	26.8
H126β	$n = 128 \rightarrow 126$	6.42158	27.6
H127β	$n = 129 \rightarrow 127$	6.27223	25.8
H128β	$n = 130 \rightarrow 128$	6.12748	26.3
H129β	$n = 131 \rightarrow 129$	5.98714	25.2
H130β	$n = 132 \rightarrow 130$	5.85107	23.7
H131β	$n = 133 \rightarrow 131$	5.71909	23.3
H132β	$n = 134 \rightarrow 132$	5.59105	23.8
H133β	$n = 135 \rightarrow 133$	5.46680	22.5
H134β	$n = 136 \rightarrow 134$	5.34619	23.4
H135β	$n = 137 \rightarrow 135$	5.22913	21.0
H136β	$n = 138 \rightarrow 136$	5.11544	24.0
H138β	$n = 140 \rightarrow 138$	4.89778	24.7
H139β	$n = 141 \rightarrow 139$	4.79357	24.6
H138γ	$n = 141 \rightarrow 138$	7.26889	128.5
H139γ	$n = 142 \rightarrow 139$	7.11476	59.4
H140γ	$n = 143 \rightarrow 140$	6.96495	33.3
H141γ	$n = 144 \rightarrow 141$	6.81933	33.9
H143γ	$n = 146 \rightarrow 143$	6.54004	26.4
H144γ	$n = 147 \rightarrow 144$	6.40609	25.4
H146γ	$n = 149 \rightarrow 146$	6.14898	23.6
H147γ	$n = 150 \rightarrow 147$	6.02558	25.1
$H_2^{13}CO$	1(1, 0) → 1(1, 1)	4.59309[a]	25.9
H_2CO	1(1, 0) → 1(1, 1)	4.82966	24.5
CH_3OH_3	3(1, 2) → 3(1, 3)	5.00533[a]	24.3
CH_2NH	1(1, 0) → 1(1, 1)	5.28981	24.6
HC_5N	$J = 2 \rightarrow 1$	5.32533	24.0
CCS	$N = 3 \rightarrow 2$, $J = 2$	5.40260	22.8
C_3S	$1 \rightarrow 0$	5.78076	23.4
HC_9N_2	$10 \rightarrow 9$	5.81036	23.5
CH_3OH	5(1, 5) → 6(0, 6)	6.66852	30.4
HCN	$J = 5$, $l = 1e \rightarrow 1f$	6.73191	32.5

Note.
[a] $H_2^{13}CO$ and CH_3OH_3 share their spectral windows with H141β centered at 4.59384 GHz and H137β centered at 5.00502 GHz, respectively; we do not use the H141β and H137β lines in our analyses.

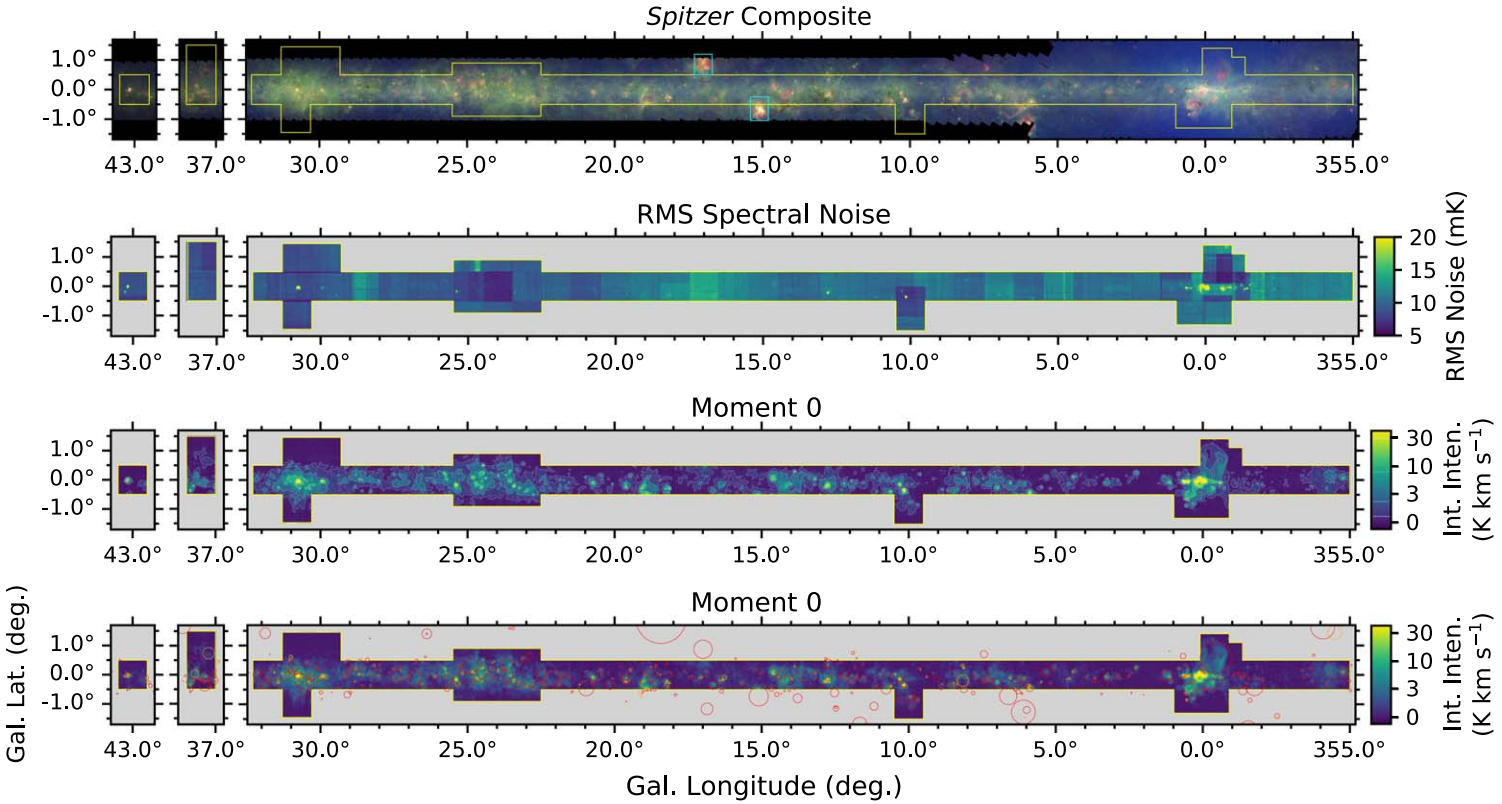

Figure 1. GDIGS areal coverage and intensity. In all panels, the yellow line shows the full GDIGS survey range. The nominal latitude range is $|b| < 0.^{\circ}5$, with additional latitude coverage near W47 at $\ell \simeq 37^{\circ}$, the giant H II region W43 (Luisi et al. 2020), the Galactic center, $\ell \simeq 10^{\circ}$, and $\ell \simeq 24^{\circ}$. Top: Spitzer data, with MIPSGAL (Carey et al. 2009) 24 μm data in red, GLIMPSE (Benjamin et al. 2003; Churchwell et al. 2009) 8.0 μm data in green, and GLIMPSE 3.6 μm data in blue. In general, the regions of stronger 8.0 μm emission indicate intense radiation fields (Luisi et al. 2017, their Figure 11), and H II regions can be identified by the red 24 μm emission surrounded by green 8.0 μm emission (Anderson et al. 2014). The cyan boxes denote coverage of M16 and M17 that are not part of the current data release but were observed in the GDIGS configuration as part of the SOFIA Legacy project "FEEDBACK" (see Appendix B). Top middle: spectral noise (rms) in the Hnα GDIGS data. We compute the rms per 30″ pixel with 0.5 km s^{-1} channels; performing this calculation for 5 km s^{-1} channels should decrease the rms by a factor of 3.2. Top bottom: GDIGS Hnα integrated intensity (Moment 0) data. Contours are at 0.5, 2, 8, and 30 K km s^{-1}. One can convert from integrated intensity to EM using Equation (2). Bottom: same as the above integrated intensity panel, but with known H II regions from the WISE Catalog overlaid in red and "group" H II regions that appear to be associated with known regions in orange.

nominal longitude zone of the survey to map extended H II regions and trace bright diffuse ionized gas above and below the midplane; these areas are located near W31 ($\ell \simeq 10°$), $\ell = 24°$, and W43 ($\ell \simeq 30°$; Luisi et al. 2020). We describe additional mapped areas not included in this data release in Appendix B.

For the majority of the survey area, the default field size is 1 deg^2. We take data in on-the-fly (OTF) mode, slewing at 54″ s^{-1}, with rows spaced every 40″ (0.39–0.25 beams for the usable frequency range), and record data every 0.38 s, or 20″ (0.19–0.12 beams). The row spacing is greater than the Nyquist rate at the highest usable frequency of 7.3 GHz. We observe each field in four coverages, making two complete maps by scanning in Galactic longitude and two more by scanning in Galactic latitude. This redundancy reduces the impact of temporal artifacts such as weather. For each of the four coverages, the integration time per beam is 4.6–11 s, and therefore, the total integration time per beam is 19–45 s.

We observe a reference position every 16 rows, or ∼20 minutes, using integration times of 66.6 s (the duration of one row). This strategy ensures that all data in the map are taken within ∼10 minutes of observing a reference position. The reference positions are nominally 3° above the plane at the Galactic longitude of the field center. We verify that each reference position is free of RRL emission prior to beginning a map by performing pointed observations at each position. The pointed observations use the same setup as the OTF maps, with on- and off-source integration times of 6 minutes each. The off-source scans track the same azimuth and zenith angle path as the on-source scans such that they follow the same path on the sky. The typical rms spectral noise in the pointed observations is ∼1.5 mK (0.75 mJy beam^{-1}) after averaging all Hnα lines and smoothing to 1.86 km s^{-1} velocity resolution. If emission is detected, we adjust the reference location and repeat the pointed observations prior to beginning the OTF maps.

2.3. Calibration

We calibrate the intensity scale of the data using two methods but make no correction for elevation or weather. We first calibrate the intensity scale using noise diodes fired during data acquisition, a method that from experience has ∼10% uncertainties (Anderson et al. 2011).

We also calibrate the intensity scale using the standard source 3C 286, for which the flux density and spectral index are well known. We periodically (approximately every two months) map 3C 286 using our same OTF mode and backend configuration; we make 14 maps in total. As 3C 286 is a nonthermal source, we do not measure spectral lines, only the total-power continuum. The use of 3C 286 as a calibrator therefore assumes that the continuum and line responses can both be calibrated using total-power continuum observations. We determine the intensity of 3C 286 in each map at each spectral window and polarization by measuring the amplitude of a two-dimensional Gaussian fit (which necessarily removes any spatial baseline).

We average the measured 3C 286 intensity of the 14 maps at each spectral window and polarization and compute the deviations from the expected intensity in Ott et al. (1994). These deviations are up to ∼10% using the gain of 2.0 K Jy^{-1} (see Figure 2, top panel). We compute intensity corrections from the differences between the measured and expected values, which we then apply to all individual spectral windows and polarization maps. The standard deviation in the 3C 286 intensities from the 14 individual spectral window and polarization maps has values of 1.5%–2.0% or 0.2 K, increasing with frequency, which gives some indication of the variations due to weather, elevation, and electronics stability (see Figure 2, middle and bottom panels).

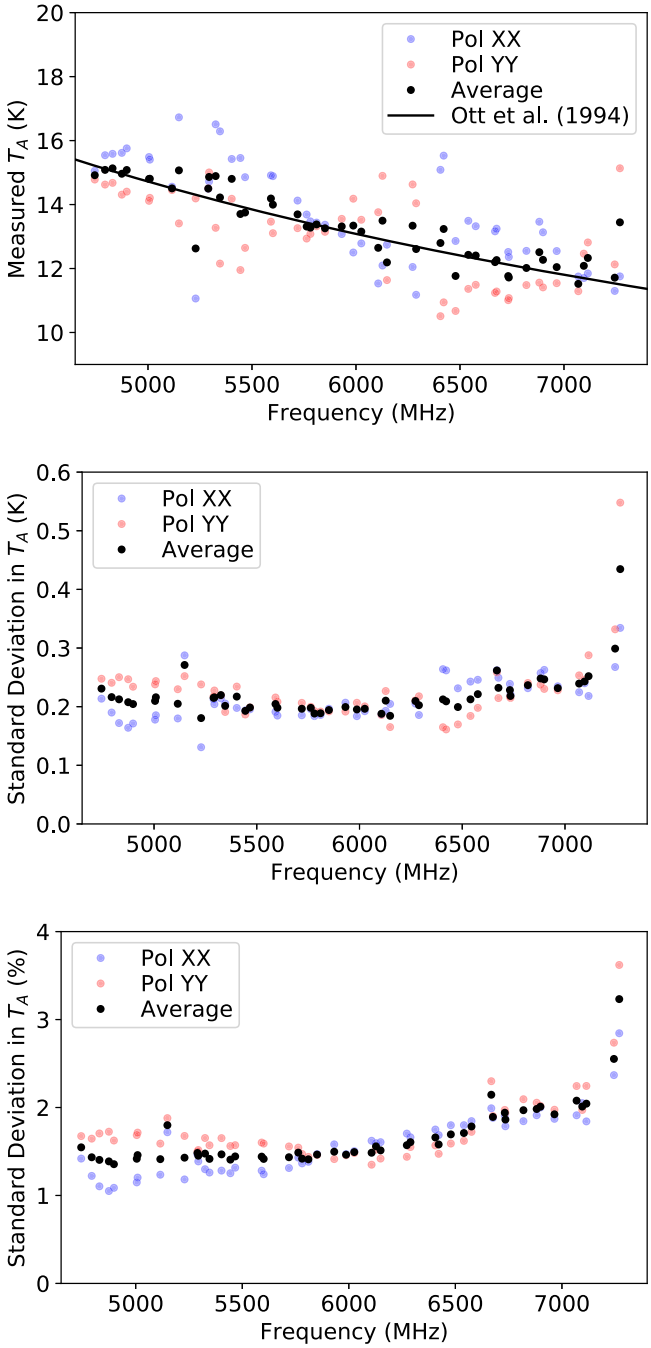

Figure 2. Top: measured antenna temperatures of 3C 286 for each spectral window and polarization prior to flux calibration. The antenna temperature values are averaged over all 14 observations of 3C 286. The intensities of the individual polarization spectral windows show considerable deviations from the expected flux density of 3C 286 (Ott et al. 1994, indicated by the black line), although much of this discrepancy disappears in the polarization-averaged data. Middle: standard deviations in antenna temperature between all 14 maps of 3C 286. Bottom: same, but showing the relative standard deviations. The standard deviation averaged over all tunings is 1.7%.

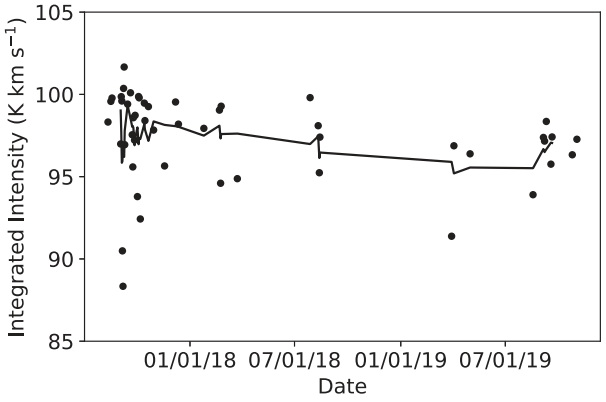

Figure 3. Hnα integrated intensity of W43 as a function of observation date. The solid black line shows the moving average of the data with a subset size of 6. The standard deviation of all data is 3.6% of the average value. The apparent decrease in integrated intensity with time is not statistically significant ($p = 0.09$).

Finally, to verify the stability of the spectral line intensity scale under the variety of observing conditions encountered, we periodically measure the average Hnα emission from the giant H II region W43 (see Luisi et al. 2020). We observe W43 at the beginning of most observing sessions, using pointed observations with the same backend setup. For each observation, we average all usable Hnα transitions together, resample to a common velocity resolution of 1.86 km s^{-1}, and fit a single Gaussian line profile. Figure 3 shows the integrated Hnα intensities of all observations of W43. The distribution of observed integrated Hnα intensities has a standard deviation of 2.8%; the distribution of Hnα intensities of W43 (not shown) has a standard deviation of 3.6%.

The overall uncertainty in the intensity of the Hnα data, computed as the combination of absolute calibration and temporal uncertainties, is ∼5%. We expect that the intensities of the average Hnβ and Hnγ maps have similar uncertainties. The pointed W43 data show that temporal effects lead to uncertainties in the average Hnα data at the level of $\lesssim$ 4%. From the standard deviation of the 3C 286 data measured at each spectral window and polarization, the uncertainty is ∼2%. The temporal and absolute calibration effects are not entirely independent, as the mean value for the W43 integrated intensity is affected by the absolute calibration of the data. The estimated ∼5% uncertainty is in between the value obtained from independent (4.5%) and dependent (6%) absolute intensity and temporal uncertainties.

2.4. RFI Removal

Transitory radio frequency interference (RFI) can spoil entire spectra or cause abnormal spectral features in otherwise good spectra. We design two RFI mitigation techniques to remove spectra spoiled by RFI and to remove the strongest RFI signals from spectra that are otherwise usable. For a given single-frequency and polarization spectrum, the first technique compares the rms of the line-free portions of the spectrum (approximately −350 to −175 km s^{-1} and +175 to +350 km s^{-1}, using a narrower velocity range near the Galactic center) with the expected noise level from the radiometer equation that we calculate from the measured system temperature. We remove entire spectra that have rms values that are five times greater than that expected from the radiometer equation.

In our second RFI removal operation, we first apply a median absolute deviation (MAD) filter to the data in each spectral window. We remove data points that have absolute intensities $>6 \times$ MAD, where MAD is computed in a sliding 101 channel window, and replace them with the median value over the same window. Because some low-intensity persistent RFI may still remain in the spectral window of the H104α line at high velocities, we apply the same MAD filter with a more aggressive $2 \times$ MAD threshold to the H104α data over the velocity range 125–200 km s^{-1}.

2.5. Map Making

Our goal is to produce average Hnα, Hnβ, and Hnγ maps with relatively uniform properties across the survey area. The GBT spatial and spectral resolutions vary over the usable frequency range, so we must grid the data into cubes that have common spatial and spectral resolutions.

We use the gbtgridder[11] software to grid the RFI-removed spectra into single spectral window and polarization data cubes, with 30″ square pixels. There are 32–13 pixels per beam for the usable frequency range. The gbtgridder algorithm uses a Gaussian kernel, following the recommendations of Mangum et al. (2007). The native data cubes output from gbtgridder have a third axis of frequency. We transform the third axis into units of velocity and resample to a uniform channel spacing of 0.5 km s^{-1} using sinc interpolation (see Wenger et al. 2021) and a uniform velocity range of −300 to +300 km s^{-1}. The gbtgridder algorithm automatically removes the median value of each spectrum; we additionally subtract a third-order polynomial baseline from each spectrum in the cubes determined from channels in the range −300 to −200 km s^{-1} and +200 to +300 km s^{-1}. If RFI is still present in the cubes after our mitigation techniques, we manually remove affected spectra and rerun gbtgridder.

The advantage of observing a large number of transitions simultaneously is that we can average all lines at a given position to make one sensitive spectrum (Balser 2006), a technique that is well understood (Anderson et al. 2011; Liu et al. 2013; Alves et al. 2015; Luisi et al. 2018). We smooth the individual maps to the resolution of the lowest frequency (4.74418 GHz for Hnα, 2.′65 FWHM Gaussian kernel; 4.79457 GHz for Hnβ, 2.′62; and 6.02558 GHz for Hnγ, 2.′09), and then average the individual maps pixel by pixel using a weighting factor of $T_{\rm sys}^{-2}$. Finally, we average the two individual polarization data cubes. This process creates average Hnα, Hnβ, and Hnγ data cubes at each spectral window.

Over the range 4.7–7.3 GHz, we expect the RRL intensity to vary by ∼60% (see Equation (A7)). For example, ignoring beam size effects, the intensity of the H111α line (in kelvin) at 4.74418 GHz will be 60% higher than the intensity of the H97α line at 7.09541 GHz. Taking into account the intensity variation with frequency and the $T_{\rm sys}^{-2}$ weighting we do when averaging, for average system temperatures at each spectral window the mean intensity-weighted frequency of the Hnα lines is 5.7578 GHz, which is near the frequency of the H104α line. The mean intensity-weighted frequencies of the Hnβ and Hnγ lines are 5.7959 GHz (in between H130β and H131β) and 6.4528 GHz (nearest to H144γ), respectively.

From these intensity-weighted frequencies, we can compute the expected intensity ratios of the α, β, and γ maps using

[11] https://github.com/GreenBankObservatory/gbtgridder

Equation (A7), assuming local thermodynamic equilibrium (LTE). Ignoring beam size effects, the average Hnβ maps should have intensity values 28% that of the Hnα maps; the average Hnγ maps should have intensity values 12% that of the Hnα maps, or 43% that of the Hnβ maps.

2.6. Primary Data Products

The primary GDIGS RRL data products discussed here are maps of the average Hnα, Hnβ, and Hnγ emission with 30″ pixels, 0.5 km s^{-1} spectral resolution, and $\pm$300 km s^{-1} velocity coverage. We also produce polarization-averaged maps of each individual Hnα, Hnβ, and Hnγ transition (H97α to H111α; H121β to H139β, excluding H137β; H138γ to H147γ). These data, as well as data from the related projects (see Appendix B), can be downloaded from our project website.[12] For each data product, we produce 1 deg^2 maps, and also larger maps spanning 6° in longitude that overlap adjacent maps by 0.°5 on the high- and low-longitude sides. If one Hnα line has severe data quality issues, it is removed from the entire map. If a given 1 deg^2 map has a compromised Hnα line, all data from the line are excluded when creating the 1 deg^2 map and also when creating the corresponding map that spans 6° in longitude. The sensitivity of the larger maps can thus be slightly lower than that of the 1 deg^2 maps, typically by a few percent. For this reason, we recommend all studies of individual regions be performed with the 1 deg^2 maps.

We show the integrated intensity (Moment 0) GDIGS Hnα data in the bottom two panels of Figure 1. To create this map, we regrid to a velocity resolution of 15 km s^{-1}. For each spaxel, we then sum the emission from those velocity channels that have intensities greater than three times the rms spectral noise of that spaxel (see below). One can convert from the integrated intensity value shown in the image to EM using Equation (2). Figure 4 provides an alternate view of the Hnα data, with intensity in channels 20 km s^{-1} wide. Galactic rotation is evident in Figure 4, as the emission peaks at low Galactic longitudes at low velocities and higher Galactic longitudes at higher velocities. Finally, in Figure 5, we show an Hnα longitude–velocity diagram of the contiguous GDIGS zone, made by integrating over the complete latitude coverage. This figure demonstrates that RRL emission is detected over the entire survey zone and that the emission follows that of the H II region distribution.

We compute the rms spectral noise over velocities -300 to -150 km s^{-1} and $+200$ to $+300$ km s^{-1} and display the Hnα noise map in Figure 1. In the portion of the Galaxy observed by GDIGS, there should be almost no Galactic Hnα emission in this velocity range. The one major exception is for Sgr E (Liszt et al. 1981; Cram et al. 1996), for which we only use the positive velocity range when computing the rms. The noise is relatively uniform across the survey, but map edges and discrete locations of relatively high noise in the direction of bright continuum sources are apparent.

For the entire survey, the mean and mode of the Hnα rms spectral noise distribution as computed from the large cubes that span 6° in Galactic longitude are ~10 mK (10.3 mK and 10.0 mK, respectively; see Figure 6). An rms of 10 mK is equivalent to 5 mJy beam^{-1} or ~1800 cm^{-6} pc. Locations of high noise are found toward bright continuum sources, most notably at the location of W43 ($\ell \simeq 31°$) and Sgr A* ($\ell = 0°$). Figure 6 shows that the noise also gradually increases at low Galactic longitudes, as a result of the low observing elevations. The mean spectral noise in the Hnβ maps is similar to that of the Hnα maps (10.8 mK), whereas due to the smaller number of RRLs, that of the Hnγ maps is ~100% higher (21.3 mK). Because RRLs are ~25 km s^{-1} wide, we can smooth to 5 km s^{-1} resolution without loss of information. This smoothing should reduce the noise by a factor of 3.2. Spatial smoothing can reduce the noise further.

We can relate the 10.3 mK rms noise level to the properties of ionized gas using Equation (1). From Equation (1) of Lenz & Ayres (1992), a 3σ detection requires a line intensity of 6.2 mK, for a line width of 25 km s^{-1} and an rms noise level of 10.3 mK. Using Equation (2), this corresponds to EM $\simeq$ 1100 cm^{-6} pc. GDIGS is therefore sensitive to the Hnα RRL emission from H II regions with path lengths of 1 pc and mean densities of $\langle n_e \rangle \gtrsim 30$ cm^{-3} (using Equation (1)). If the H II region path length is 10 pc, GDIGS can detect plasma with $\langle n_e \rangle \gtrsim 10$ cm^{-3}. For the DIG, if we assume a 1 kpc path length, GDIGS can detect plasma with $\langle n_e \rangle \gtrsim 1$ cm^{-3}. All values assume line widths of 25 km s^{-1} and electron temperatures of 8000 K; the EM value that GDIGS is sensitive to will increase for narrower lines and/or higher electron temperatures (and hence so too will the values of $\langle n_e \rangle$).

3. Enhanced Data Products

Here, we describe and briefly characterize two enhanced data products provided for the community: maps resulting from automatic Gaussian decomposition and "DIG-only" data cubes. The science enabled by these data products will be the subject of future papers in this series.

3.1. Automatic Gaussian Decomposition

A Gaussian decomposition of the GDIGS data allows us to study the RRL properties across the survey area. We fit Gaussian profiles to the Hnα GDIGS data using the "GaussPy +" algorithm (Riener et al. 2019). This algorithm decomposes the spectral data into one or more Gaussian components for each spaxel that has a detection above the 3σ level, where the rms is evaluated independently for each spaxel. We restrict the fits to have FWHM values above 5 km s^{-1}, which removes spurious fits to any residual RFI while retaining real signals (see Anderson et al. 2011, their Figure 8). We also filter out any He RRL decompositions by removing fits whose peak velocities are offset -130 to -110 km s^{-1} from the peak velocities of brighter components at the same spaxels. We show representative Hnα spectra and their automatic Gaussian fits in Figure 7.

In Figure 8, we show histograms of the FWHM line widths, peak line intensities, and integrated line intensities obtained from this Gaussian decomposition, as well as a scatter plot of line intensity versus line width. In each histogram, we indicate the median (in blue) and mode (in red) of the distribution. The FWHM and integrated line intensity distributions are approximately log-normal, while the peak intensity has a high-intensity tail. Although FWHM values $\gtrsim$60 km s^{-1} are not seen toward discrete H II regions (e.g., Anderson et al. 2011), we believe the highest FWHM values in Figure 8 are real, as they are mainly found toward the Galactic center where we expect broad lines due to the gas motions (e.g., Lockman & Gordon 1973; Geballe et al. 1987). The FWHM versus intensity scatter plot shows no

[12] http://astro.phys.wvu.edu/gdigs/

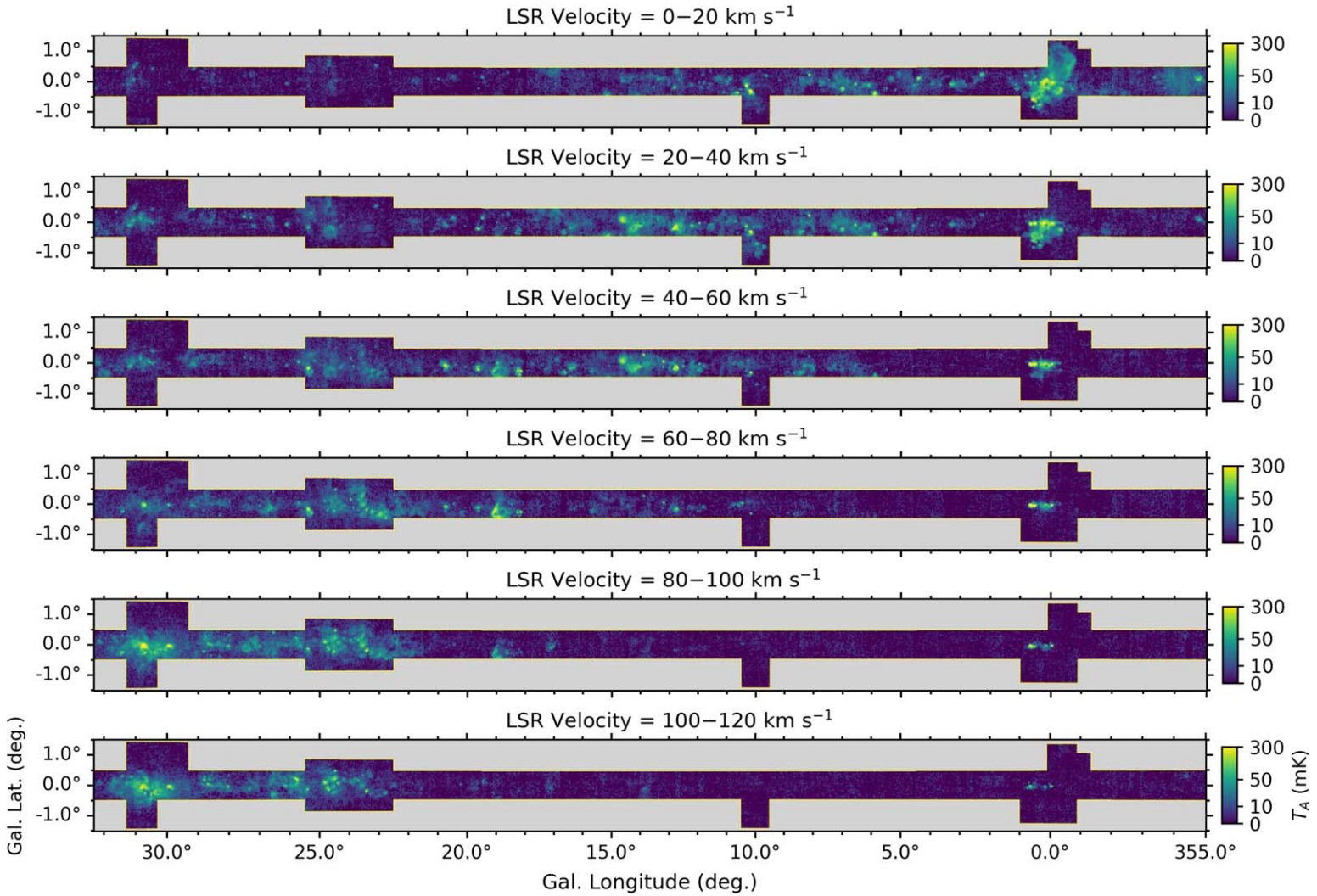

Figure 4. GDIGS Hnα emission in the large contiguous coverage area for local standard of rest (LSR) velocities between 0 and 120 km s^{-1}, in 20 km s^{-1} increments, smoothed to 2.′5 resolution. The intensity scale is inverse hyperbolic sine and ranges from 0 to 300 mK. Due to Galactic rotation, the peak of the emission shifts from lower Galactic longitudes at lower velocities to higher Galactic longitudes at higher velocities. RRL emission is especially broad in the Galactic center, and so emission in that region is visible in all panels.

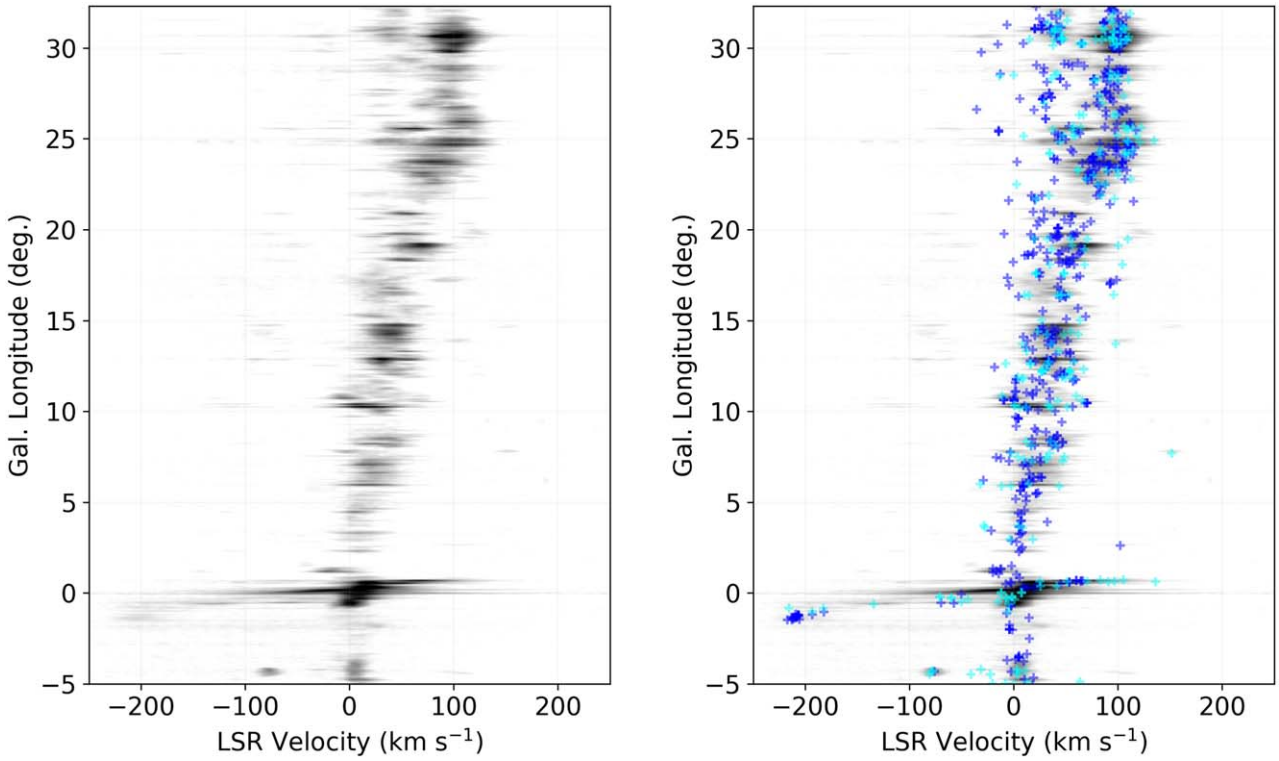

Figure 5. Longitude–velocity diagrams of the GDIGS Hnα data, in grayscale, made by integrating over all latitudes. The scale is linear from 0 to 10 K and is the same in both panels. Helium RRLs are evident, shifted by ~ -120 km s^{-1} from that of hydrogen, at $\sim$10% the intensity. The right panel overlays the positions of H II regions from the WISE Catalog, with single-velocity H II regions in blue and those with multiple detected RRL velocities in cyan. Emission at velocities devoid of H II regions is likely from the DIG.

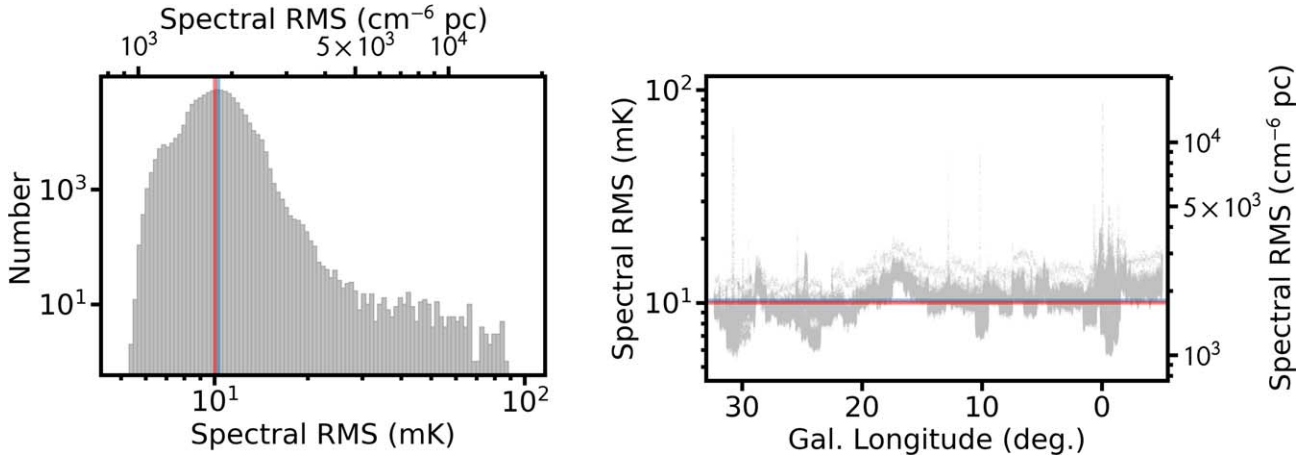

Figure 6. GDIGS Hnα spectral rms noise. Left: the rms distribution over large contiguous regions of the survey (excluding areas around W47 and W49). Both the mean (blue lines) and mode (red lines) are near 10 mK (5 mJy beam^{-1}; 1100 cm^{-6} pc). Right: the rms noise as a function of Galactic longitude. The noise increases slightly at lower Galactic longitudes as a result of low observing elevations. The noise for 5 km s^{-1} channels would decrease by a factor of 3.2 from the values shown.

strong relationship between the quantities, but the brightest spectra have FWHM values >20 km s^{-1}, and the narrowest lines are likely to be of low intensity.

Using results from the automatic Gaussian decomposition, we also produce reconstructed data cubes. For each spaxel with an automated fit, we fill the voxels of the reconstructed cubes using the fitted Gaussian parameters. We then integrate the reconstructed cubes over all latitudes to create the longitude–velocity diagram in Figure 9. Figure 9 shows that the Gaussian decomposition recovers nearly all of the GDIGS Hnα emission and that there is good agreement between the decomposed GDIGS Hnα data and the locations of discrete H II regions.

3.2. DIG-only Data Cubes

To facilitate analyses of the ionized gas components detected by GDIGS, we decompose the RRL intensity into emission from discrete H II regions and diffuse ionized gas. We can separate these components using data from the WISE Catalog of Galactic H II Regions (Anderson et al. 2014, hereafter WISE

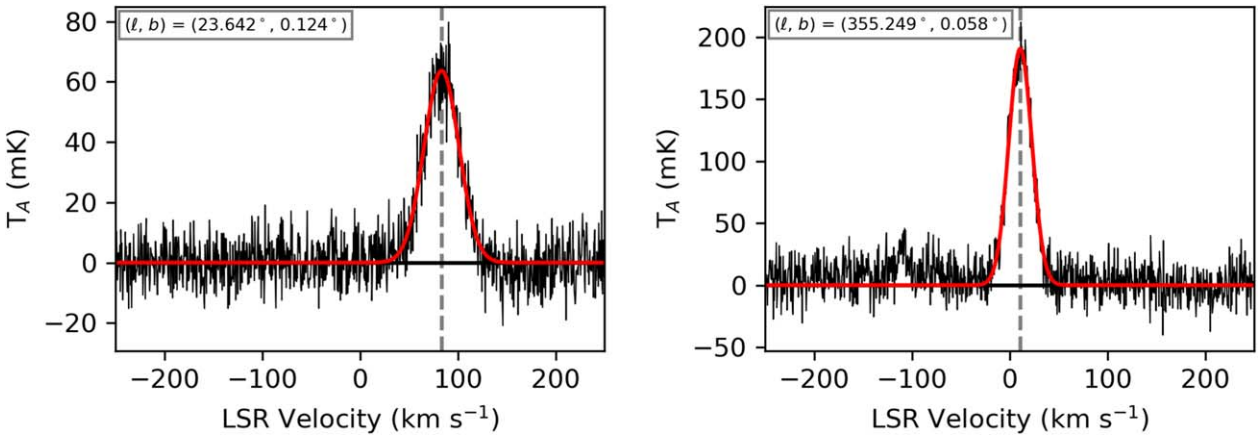

Figure 7. Example Hnα GDIGS spectra toward a position devoid of known H II regions, $(\ell, b) = (22.^{\circ}642, 0.^{\circ}124)$ (left), and toward the H II region G355.243 +00.096, $(\ell, b) = (355.^{\circ}249, 0.^{\circ}058)$ (right). Each spectrum is from a single GDIGS spaxel. The automatic Gaussian decompositions are shown in red and the fitted central velocities are indicated with dashed vertical lines. The He line is detected in the right panel at ~ -120 km s^{-1} but is excluded from the fits.

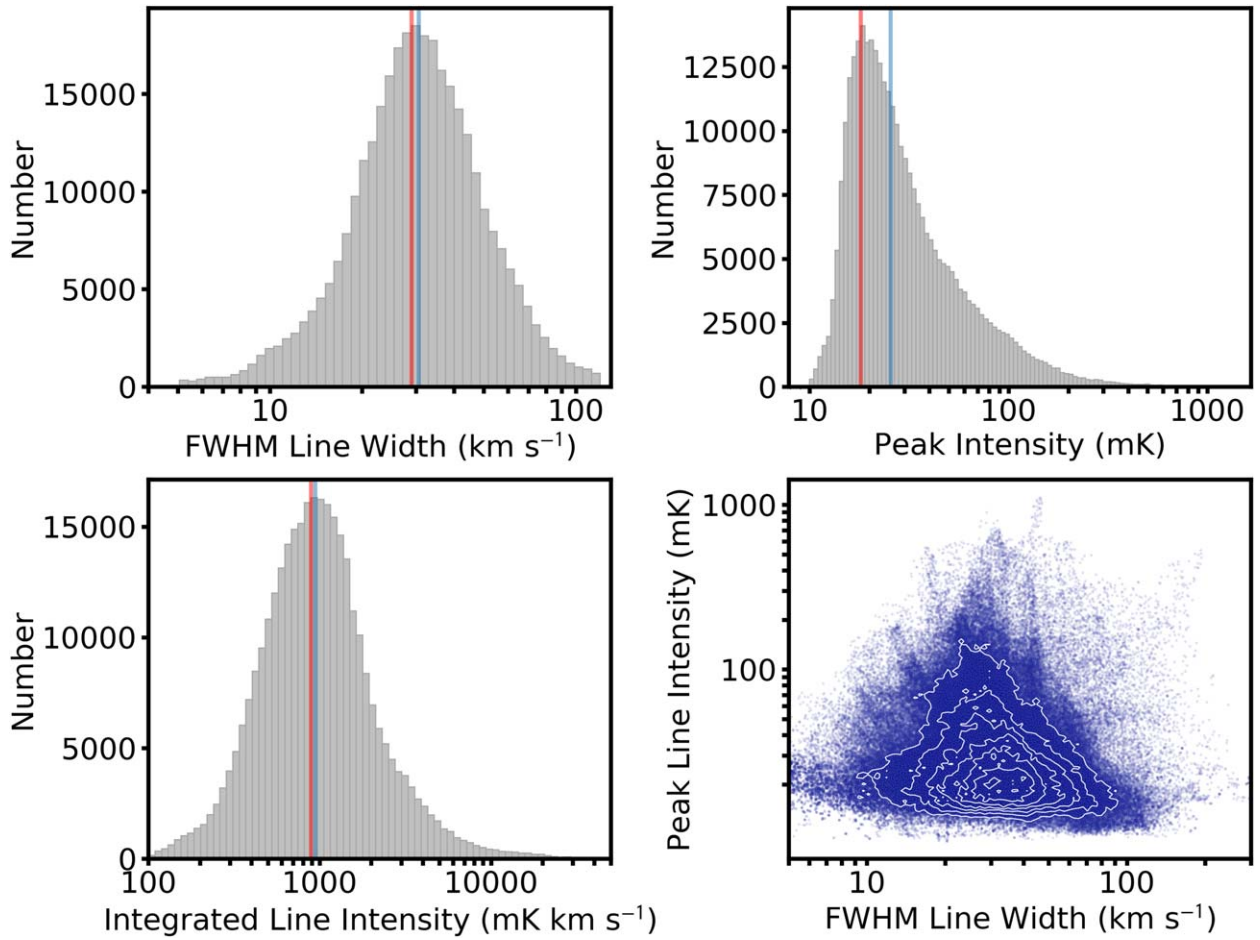

Figure 8. Fit parameters from the automatic Gaussian decomposition. Top left: FWHM line-width distribution. The median is 30.6 km s^{-1} and the mode is 29.0 km s^{-1}. Here, and in the other histograms of this figure, the median values are indicated by blue vertical lines and the mode by red vertical lines. Top right: peak intensity distribution. The median is 26 mK and the mode is 18 mK. Bottom left: integrated line intensity distribution. The median is 940 mK km s^{-1} and the mode is 890 mK km s^{-1}. Bottom right: peak line intensity vs. FWHM line width. There is no obvious correlation between the two parameters.

Catalog). The WISE Catalog is statistically complete for all H II regions powered by O stars (Mascoop et al. 2021) and so should allow for a nearly complete census of the discrete H II regions detected by GDIGS.

The WISE catalog has three main designations: known H II regions with measured ionized gas spectroscopic velocities, candidate H II regions that have the mid-infrared (MIR) morphology of H II regions and radio continuum emission, and radio-quiet candidates that have MIR morphology but lack detected radio continuum emission. A fourth category, "group" H II regions, contains the H II regions of larger complexes that were not measured in RRL emission individually. The locations

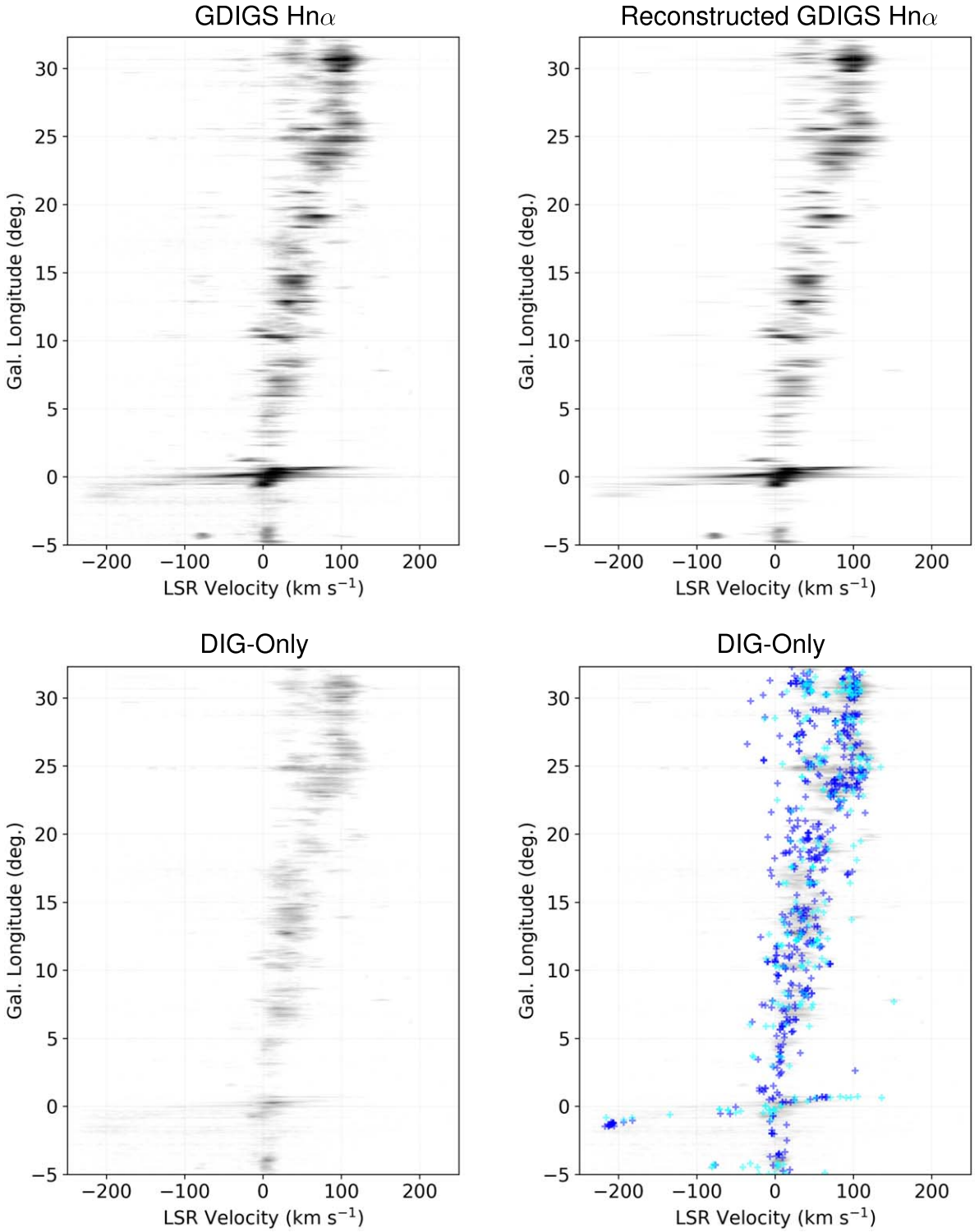

Figure 9. Longitude–velocity diagrams of the two enhanced data products, again integrated over all latitudes. As in Figure 5, the scale is linear, ranging from 0 to 10 K, and is the same in all panels. The top-left panel reproduces GDIGS Hnα RRL data from Figure 5. The top-right panel shows reconstructed GDIGS Hnα RRL data produced from the automatic Gaussian decomposition. The helium RRLs, which are offset ~ -120 km s^{-1} from that of hydrogen, have not been included in the automatic decomposition. Comparison between these two top panels shows that the Gaussian decomposition recovers the bulk of GDIGS emission. The bottom two panels show DIG-only data, without H II regions (left) and with (right), plotted in blue and cyan as in Figure 5. The DIG emission closely follows the distribution of H II regions.

and angular sizes of H II regions in the WISE Catalog were determined visually from MIR emission, including the emission of their PDRs. Because PDRs are predominantly neutral, angular sizes from the WISE Catalog are typically larger than the sizes of the fully ionized H II regions (Bihr et al. 2016).

We create "DIG-only" Hnα data cubes devoid of emission from discrete H II regions using the H II region locations, angular sizes, line widths, and velocities from the WISE catalog. For "known" H II regions, we remove emission from all GDIGS Hnα voxels at the measured H II region Hnα

velocity within ± 1.5 times the measured Hnα FWHM line width, for all spaxels that lie within the region (including pixels touching the H II region boundary). We also remove potential helium RRLs using the same line-width and location criteria, but with the velocity shifted by -122 km s^{-1} from that measured in hydrogen RRLs. Assuming a Gaussian velocity profile, the intensity at ± 1.5 times the FWHM is $\sim$0.2% of the peak intensity. This cutoff ensures that any remaining emission from discrete H II regions lies below our sensitivity threshold for a single-velocity channel. For H II region candidates, radio-quiet candidates, and "group" H II regions, we remove emission at all velocities, because we do not know the velocities of the regions. This may result in the loss of DIG emission because diffuse gas potentially lies along the same line of sight as the H II region candidates. The DIG-only cubes are available on the GDIGS website and were first shown for the massive star-forming region W43 in Luisi et al. (2020), their Figure 9. The processing here produces data that are more sensitive by a factor of $\sim$2 over those of Luisi et al. (2020), and therefore the data shown here supercede those of that paper.

We show the longitude–velocity diagram of these DIG-only data in Figure 9. The DIG-only data lack the highest intensities (darker regions in the figures), which are due to discrete H II regions. The DIG emission shows excellent spatial agreement with the loci of H II regions, indicating the close relationship between H II regions and the DIG. We will explore the nature of this relationship in a future paper.

4. Summary

GDIGS is a survey of ionized gas in the Galactic midplane. It maps the C band (4–8 GHz) RRL emission over $32\overset{\circ}{.}3 > \ell > -5°$, $|b| < 0\overset{\circ}{.}5$, with extended coverage above and below the plane in select fields and additionally covers W47 (around $\ell = 37\overset{\circ}{.}5$) and W49 (around $\ell = 43°$). The current data release concerns the Hnα, Hnβ, and Hnγ lines.

This paper characterized the GDIGS RRL data and described enhanced data products that we provide to the community. The gridded GDIGS data have a pixel size of 30″ and a channel width of 0.5 km s^{-1}. The Hnα data have a spatial resolution of $2\overset{\prime}{.}65$, whereas the Hnβ and Hnγ data have spatial resolutions of $2\overset{\prime}{.}62$ and $2\overset{\prime}{.}09$, respectively. The average spectral noise in the Hnα data cubes is 10 mK (5 mJy beam^{-1}), or $\sim$1100 cm^{-6} pc assuming an electron temperature $T_e = 8000$ K and a line width of 25 km s^{-1}.

GDIGS gives us the clearest view yet of the large-scale distribution of ionized gas in the Milky Way. Future papers in this series will examine the distribution of the DIG, the interplay between the DIG and discrete H II regions, and the association between ionized gas and other components of the ISM. These projects will shed new light on the properties of ionized gas in our Galaxy and its connection to high-mass star formation.

This work is supported by NSF grant AST1516021 to L.D.A. The Green Bank Observatory is a facility of the National Science Foundation operated under cooperative agreement by Associated Universities, Inc. We thank the staff at the Green Bank Observatory for their hospitality and friendship during the observations and data reduction. We thank West Virginia University for its financial support of GBT operations, which enabled some of the observations for this project.

Facility: Green Bank Telescope.

Software: AstroPy (Astropy Collaboration et al. 2013; Price-Whelan et al. 2018), GBTIDL[13] (Marganian et al. 2013), gbtgridder,[14] GaussPy+ (Riener et al. 2019).

Appendix A
RRL Emission

RRLs are produced in an ionized medium after an electron and an ion recombine. The recombined atom (or ion if it was multiply ionized) can be in an excited state and will emit RRLs as the electron cascades down the atomic levels toward the ground state. The hydrogen RRL photons are at frequencies

$$\nu_0 = R_M c \left[\frac{1}{n^2} - \frac{1}{(n + \Delta n)^2} \right], \tag{A1}$$

where R_M is the Rydberg factor for atoms of mass M, c is the speed of light, n is the principal quantum number of the final state, and Δn is the change in principal quantum number.

Transitions between adjacent energy levels, $\Delta n = 1$, are referred to as α lines—e.g., H89α is the hydrogen $n = 90 \rightarrow n = 89$ transition. Transitions spanning two levels, $\Delta n = 2$, are referred to as β lines; transitions spanning three levels, $\Delta n = 3$, are γ lines, etc. (Lilley et al. 1966). Hydrogen α transitions with principal quantum numbers $n \gtrsim 40$ are in the radio regime. For $n \gtrsim 40$ and $\Delta n \ll n$, Equation (A1) becomes

$$\nu_0 \approx \frac{2(R_M c)\Delta n}{n^3}. \tag{A2}$$

The spacing between adjacent lines with the same Δn is then

$$\nu_0(n) - \nu_0(n-1) \approx -2R_M c \Delta n \frac{1}{n^3 - (n-1)^3} \approx -\frac{3\nu_0}{n}. \tag{A3}$$

Therefore, RRLs are spaced closer together at lower frequencies.

For Hnα lines, the line center intensity of optically thin emission in LTE is (Gordon & Sorochenko 2000; Wenger et al. 2019)

$$\left(\frac{T_L}{\mathrm{K}}\right) \simeq 3013 \left(\frac{T_e}{\mathrm{K}}\right)^{-3/2} \left(\frac{\mathrm{EM}}{\mathrm{cm^{-6}\,pc}}\right) \times \left(\frac{\nu_0}{\mathrm{GHz}}\right)^{-1} \left(\frac{\Delta V}{\mathrm{km\ s^{-1}}}\right)^{-1} \frac{\Delta n}{n} f_{n,n+\Delta n}, \tag{A4}$$

where T_e is the electron temperature, EM is the emission measure, ν_0 is the observed frequency, ΔV is the FWHM line width, and $f_{n,n+\Delta n}$ is the oscillator strength for transitions between levels n and $n + \Delta n$. Menzel (1968) approximates the oscillator strength as

$$f_{n,n+\Delta n} \approx n M_{\Delta n} \left(1 + 1.5 \frac{\Delta n}{n}\right), \tag{A5}$$

where $M_{\Delta n}$ has values of $M_{\Delta n} = 0.190775$, 0.026332, and 0.0081056 for $\Delta n = 1$, 2, and 3, respectively (Menzel 1968). Substituting ν_0 for n using Equation (A2) and using the

[13] http://gbtidl.nrao.edu/
[14] https://github.com/GreenBankObservatory/gbtgridder

expression for the oscillator strength in Equation (A5), we find

$$\left(\frac{T_{\rm L}}{\rm K}\right) \simeq 3013\left(\frac{T_{\rm e}}{\rm K}\right)^{-3/2}\left(\frac{\rm EM}{\rm cm^{-6}\,pc}\right)\left(\frac{\nu_0}{\rm GHz}\right)^{-1}\left(\frac{\Delta V}{\rm km\ s^{-1}}\right)^{-1} \times \Delta n M_{\Delta n}\left[1 + 0.00800\Delta n^{2/3}\left(\frac{\nu_0}{\rm GHz}\right)^{1/3}\right]. \quad \text{(A6)}$$

Because $1 + 0.00800\Delta n^{2/3}(\nu_0/\,\mathrm{GHz})^{1/3} \simeq 1.01 - 1.03$ for the frequencies and values of Δn used here, using an average value of 1.02, we find

$$\left(\frac{T_{\rm L}}{\rm K}\right) \simeq 3076\left(\frac{T_{\rm e}}{\rm K}\right)^{-3/2}\left(\frac{\rm EM}{\rm cm^{-6}\,pc}\right) \times \left(\frac{\nu_0}{\rm GHz}\right)^{-1}\left(\frac{\Delta V}{\rm km\ s^{-1}}\right)^{-1}\Delta n M_{\Delta n}. \quad \text{(A7)}$$

Assuming the line width is not a function of frequency, for a given Δn, the measured intensity decreases approximately linearly with increasing frequency. Because the flux density in Jansky follows $S_\nu \propto T_{\rm L}\nu^2$, it increases approximately linearly with increasing frequency. For a Gaussian line profile, the RRL integrated intensity $W_{\rm RRL}$ is

$$\frac{W_{\rm RRL}}{\rm K\ km\ s^{-1}} = \frac{1}{2}\left(\frac{\pi}{\ln 2}\right)^{0.5}\frac{T_L}{\rm K}\frac{\Delta V}{\rm km\ s^{-1}} \simeq 3274\left(\frac{T_{\rm e}}{\rm K}\right)^{-3/2} \times \left(\frac{\rm EM}{\rm cm^{-6}\,pc}\right)\left(\frac{\nu_0}{\rm GHz}\right)^{-1}\Delta n M_{\Delta n}. \quad \text{(A8)}$$

These relations ignore beam size effects.

Appendix B
GDIGS Website

We provide a website so users can download GDIGS data.[15] This site currently contains Hnα, Hnβ, and Hnγ data. We will continue to expand this site as more GDIGS data are published.

The website also contains data from related projects taken with the same GDIGS observing mode, calibration, and data reduction, albeit often with different mapping speeds. Table 3 lists these projects and has columns of the field name, field centroid, mapped area, and integration time per Hnα 2.′65 beam. As part of the SOFIA "FEEDBACK" Legacy project that maps [C II] emission from H II region complexes (Schneider et al. 2020), we observed fields around M17, M16, W40, DR21, and NGC 7538. We observed fields around S235 to aid the analysis of SOFIA [C II] data in Anderson et al. (2019) and around W51 to investigate the cause of high rotation measures found in this direction (Shanahan et al. 2019). Finally, we observed fields around Cygnus X and Orion as part of an ongoing effort to map the brightest star-forming regions in the Galaxy.

Table 3
Other Observed Targets

Field	ℓ (deg)	b (deg)	Area (sq. deg)	$t_{\rm int}$ (s)
M17	15.°10	−0.°70	0.42	45
M16	17.°00	0.°85	0.42	45
W40	28.°75	3.°45	0.36	45
W51	48.°94	0.°00	8.75	18
Cygnus X	79.°74	0.°88	64.00	3.8
DR21	81.°65	0.°65	0.42	36
NGC 7538	111.°60	0.°85	0.25	45
S235	173.°60	2.°70	0.56	45
Orion	209.°00	−19.°50	3.20	45

[15] http://astro.phys.wvu.edu/gdigs/

ORCID iDs

L. D. Anderson https://orcid.org/0000-0001-8800-1793
Matteo Luisi https://orcid.org/0000-0001-8061-216X
Bin Liu https://orcid.org/0000-0002-1311-8839
Trey V. Wenger https://orcid.org/0000-0003-0640-7787
Dana. S. Balser https://orcid.org/0000-0002-2465-7803
T. M. Bania https://orcid.org/0000-0003-4866-460X
L. M. Haffner https://orcid.org/0000-0002-9947-6396
Dylan J. Linville https://orcid.org/0000-0002-4727-7619
J. L. Mascoop https://orcid.org/0000-0002-3758-2492

References

Alves, M. I. R., Calabretta, M., Davies, R. D., et al. 2015, MNRAS, 450, 2025
Anantharamaiah, K. R. 1985, JApA, 6, 203
Anantharamaiah, K. R. 1986, JApA, 7, 131
Anderson, L. D., Armentrout, W. P., Luisi, M., et al. 2018, ApJS, 234, 33
Anderson, L. D., Bania, T. M., Balser, D. S., et al. 2014, ApJS, 212, 1
Anderson, L. D., Bania, T. M., Balser, D. S., & Rood, R. T. 2011, ApJS, 194, 32
Anderson, L. D., Deharveng, L., Zavagno, A., et al. 2015a, ApJ, 800, 101
Anderson, L. D., Hough, L. A., Wenger, T. V., Bania, T. M., & Balser, D. S. 2015b, ApJ, 810, 42
Anderson, L. D., Makai, Z., Luisi, M., et al. 2019, ApJ, 882, 11
Astropy Collaboration, Robitaille, T. P., Tollerud, E. J., et al. 2013, A&A, 558, A33
Bacon, R., Accardo, M., Adjali, L., et al. 2010, Proc. SPIE, 7735, 773508
Bacon, R., Copin, Y., Monnet, G., et al. 2001, MNRAS, 326, 23
Baddi, R. 2012, AJ, 143, 26
Balser, D. S. 2006, AJ, 132, 2326
Bania, T. M., Anderson, L. D., Balser, D. S., & Rood, R. T. 2010, ApJL, 718, L106
Benjamin, R. A., Churchwell, E., Babler, B. L., et al. 2003, PASP, 115, 953
Bershady, M. A., Andersen, D. R., Verheijen, M. A. W., et al. 2005, ApJS, 156, 311
Bihr, S., Johnston, K. G., Beuther, H., et al. 2016, A&A, 588, A97
Boulares, A., & Cox, D. P. 1990, ApJ, 365, 544
Bundy, K., Bershady, M. A., Law, D. R., et al. 2015, ApJ, 798, 7
Carey, S. J., Noriega-Crespo, A., Mizuno, D. R., et al. 2009, PASP, 121, 76
Churchwell, E., Babler, B. L., Meade, M. R., et al. 2009, PASP, 121, 213
Cram, L. E., Claussen, M. J., Beasley, A. J., Gray, A. D., & Goss, W. M. 1996, MNRAS, 280, 1110
Geballe, T. R., Wade, R., Krisciunas, K., Gatley, I., & Bird, M. C. 1987, ApJ, 320, 562
Geyer, M., & Walker, M. A. 2018, MNRAS, 481, 1609
Ghigo, F., Maddalena, R., Balser, D., & Langston, G. 2001, GBT Commissioning Memo 10
Goldsmith, P. F., Yıldız, U. A., Langer, W. D., & Pineda, J. L. 2015, ApJ, 814, 133
Gordon, M. A., & Sorochenko, R. L. 2000, Radio Recombination Lines (Dordrecht: Kluwer), 2002
Gunn, J. E., Siegmund, W. A., Mannery, E. J., et al. 2006, AJ, 131, 2332
Haffner, L. M., Dettmar, R.-J., Beckman, J. E., et al. 2009, RvMP, 81, 969
Haffner, L. M., Reynolds, R. J., Tufte, S. L., et al. 2003, ApJS, 149, 405
Hill, G. J., MacQueen, P. J., Smith, M. P., et al. 2008, Proc. SPIE, 7014, 701470
Hoyle, F., & Ellis, G. R. A. 1963, AuJPh, 16, 1
Kollmeier, J. A., Zasowski, G., Rix, H.-W., et al. 2017, arXiv:1711.03234
Lenz, D. D., & Ayres, T. R. 1992, PASP, 104, 1104
Lilley, A. E., Menzel, D. H., Penfield, H., & Zuckerman, B. 1966, Natur, 209, 468
Liszt, H. S., Burton, W. B., & Bania, T. M. 1981, ApJ, 246, 74
Liu, B., Anderson, L. D., McIntyre, T., et al. 2019, ApJS, 240, 14

Liu, B., McIntyre, T., Terzian, Y., et al. 2013, AJ, 146, 80
Lockman, F. J., & Brown, R. L. 1975, ApJ, 201, 134
Lockman, F. J., & Gordon, M. A. 1973, ApJ, 182, 25
Luisi, M., Anderson, L. D., Balser, D. S., Bania, T. M., & Wenger, T. V. 2016, ApJ, 824, 125
Luisi, M., Anderson, L. D., Balser, D. S., Wenger, T. V., & Bania, T. M. 2017, ApJ, 849, 117
Luisi, M., Anderson, L. D., Bania, T. M., et al. 2018, PASP, 130, 084101
Luisi, M., Anderson, L. D., Liu, B., et al. 2020, ApJ, 889, 96
Luisi, M., Anderson, L. D., Liu, B., Anish Roshi, D., & Churchwell, E. 2019, ApJS, 241, 2
Mangum, J. G., Emerson, D. T., & Greisen, E. W. 2007, A&A, 474, 679
Marganian, P., Garwood, R. W., Braatz, J. A., Radziwill, N. M., & Maddalena, R. J. 2013, GBTIDL: Reduction and Analysis of GBT Spectral Line Data, Astrophysics Source Code Library, ascl:1303.019
Mascoop, J. L., Anderson, L. D., Wenger, T. V., et al. 2021, ApJ, 910, 159
Menzel, D. H. 1968, Natur, 218, 756
Ott, M., Witzel, A., Quirrenbach, A., et al. 1994, A&A, 284, 331
Pellegrini, E. W., Reissl, S., Rahner, D., et al. 2020, MNRAS, 498, 3193
Pineda, J. L., Horiuchi, S., Anderson, L. D., et al. 2019, ApJ, 886, 1
Price-Whelan, A. M., Sipőcz, B. M., Günther, H. M., et al. 2018, AJ, 156, 123
Reynolds, R. J. 1991, in IAU Symp. 144, The Interstellar Disk-Halo Connection in Galaxies, ed. H. Bloemen (Dordrecht: Kluwer Academic), 67
Reynolds, R. J., Tufte, S. L., Haffner, L. M., Jaehnig, K., & Percival, J. W. 1998, PASA, 15, 14
Riener, M., Kainulainen, J., Henshaw, J. D., et al. 2019, A&A, 628, A78
Roshi, D. A., & Anantharamaiah, K. R. 2000, ApJ, 535, 231
Roshi, D. A., & Anantharamaiah, K. R. 2001, ApJ, 557, 226
Roth, M. M., Kelz, A., Fechner, T., et al. 2005, PASP, 117, 620
Schneider, N., Simon, R., Guevara, C., et al. 2020, PASP, 132, 104301
Shanahan, R., Lemmer, S. J., Stil, J. M., et al. 2019, ApJL, 887, L7
Wenger, T. V., Balser, D. S., Anderson, L. D., & Bania, T. M. 2019, ApJ, 887, 114
Wenger, T. V., Dawson, J. R., Dickey, J. M., et al. 2021, arXiv:2103.12199
Wright, E. L., Mather, J. C., Bennett, C. L., et al. 1991, ApJ, 381, 200